

# Learning about random media from near-surface backscattering: using machine learning to measure particle size and concentration.

Artur L Gower,<sup>1, a)</sup> Robert M Gower,<sup>2, b)</sup> Jonathan Deakin,<sup>1</sup> William J Parnell,<sup>1</sup> and I. David Abrahams<sup>3</sup>

<sup>1)</sup>*School of Mathematics, University of Manchester, Oxford Road, Manchester, M13 9PL, UK*

<sup>2)</sup>*LTCI, Télécom Paristech, Université Paris-Saclay, 75013, Paris, France*

<sup>3)</sup>*Isaac Newton Institute for Mathematical Sciences, 20 Clarkson Road, Cambridge CB3 0EH, UK*

(Dated: January 10, 2018)

We ask what can be measured from a random media by using backscattered waves, emitted from and received at one source. We show that in 2D both the particle radius and concentration can be accurately measured for particles with Dirichlet boundary conditions. This is challenging to do for a wide range of particle volume fractions, 1% to 21%, because for high volume fraction the effects of multiple scattering are not completely understood. Across this range we show that the concentration can be accurately measured just from the mean backscattered wave, but the particle radius requires the backscattered variance, or intensity. We also show that using incident wavenumbers  $0 \leq k \leq 0.8$  is ideal to measure particle radius between 0 and 2. To answer these questions we use supervised machine learning (kernel ridge regression) together with a large, precise, dataset of simulated backscattered waves. One long term aim is to develop a device, powered by data, that can characterise random media from backscattering with little prior knowledge. Here we take the first steps towards this goal.

Under close inspection, many materials are composed of small randomly distributed particles or inclusions. So it is no surprise that the need to measure these particles, such as their average size and concentration, spans many physical disciplines. For quick non-invasive measurements, waves, either mechanical, electromagnetic or quantum, are the preferred choice. However, measuring a broad range of particle concentrations and sizes is still an open challenge. For high concentration the wave undergoes multiple scattering, which requires specialised methods to compute and interpret. And further, measuring a wide range of particle sizes means a wide range of frequencies needs to be considered.

The type of wave depends on the type of particle: acoustic waves are used to measure liquid emulsions<sup>1</sup>, sediment on the ocean floor<sup>2</sup> and polycrystalline materials<sup>3</sup>. Microwaves are vital in remote sensing of ice<sup>4</sup>; optics for aerosols<sup>5</sup> and cellular components, both micrometer<sup>6</sup> and nanoscale<sup>7</sup> structures, among many other applications. Backscattered waves have been used to estimate particle properties by

- relating their Doppler shift to particle size, as in dynamic light scattering<sup>8</sup>, which is different to our case as we consider particles that move slowly in comparison to the incident wave.
- comparing them directly to theoretical predictions<sup>2,9</sup>. These methods often assume small particle concentrations so that multiple scattering can be ignored.

- inferring from them the average transmitted wave speed and attenuation<sup>10–12</sup>, which is possible when the sample is a rectangular slab with a known dimensions. These techniques are more common in transmission experiments in acoustics<sup>1</sup>.
- measuring the backscattered intensity for a range of scattering angles by using an array of receivers/sources. From this the transport mean free path and transport speed can be estimated<sup>13,14</sup>, which in turn are related to the microstructure.

Here we ask can one source/receiver measure the properties of a random media? And is it possible to do so without measuring the backscattered for a range of scattering angles, and without being restricted to a slab of material with known dimensions? Figure 1 illustrates this measurement. Though we do assume that it is possible to measure the backscattering for many different particle positions. We show that, with this simple setup, it is possible to recover a wide range of concentrations and particle radii, even including particles with a sub-wavelength radius. We also identify which part of the backscattered signal is sensitive to the concentration/particle radius. In doing so, we show that a supervised machine learning approach is an accurate and a simple way of predicting particle radius and concentration from backscattered waves. Supervised machine learning in similar contexts has already shown great promise<sup>15</sup>.

The long term goal is to develop a device, that with little prior information, can determine the micro-structure of a broad range of random media. To do so will require theoretical predictions, experiments and simulations of backscattered waves. A supervised learning approach can then easily combine data from these different sources to

---

<sup>a)</sup>arturgower@gmail.com; <https://arturgower.github.io/>

<sup>b)</sup>gowerrobert@gmail.com; <https://perso.telecom-paristech.fr/rgower/>

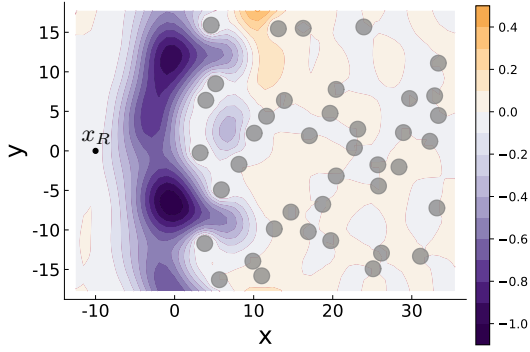


Figure 1: a snapshot of a backscattered pulse after  $t = 20$ . Initially at  $t = 0$  the plane wave pulse was centred at  $x = x_R$ , then it travelled towards the random medium, the grey particles, and then reflected back to the receiver at  $x = x_R$ . The colour indicates the wave amplitude. The particles occupy 10% of the volume and have radius 1. In practice around 150 particles were used for these parameters.

produce an algorithm that predicts the media's micro-structure. Here we take the first step towards this goal, by using simulated data, as it is the most accurate for a broad range of media.

The most common approach to determine the micro-structure from backscattering, to date, is to adjust the parameters of a theoretical model until it fits the measured backscattering. Ideally, these two approaches could be combined to produce a more accurate method valid for a larger range of parameters.

**Simulating backscattering** — We consider a simple setting with Dirichlet boundary conditions, that is, where the scalar wave-field  $u = 0$  on the boundary of the particles, which for acoustics corresponds to zero pressure, and for electromagnetism corresponds to zero electric or magnetic susceptibility, depending on the polarisation. This case is particularly challenging for many of the theoretical approaches, as they lead to unphysical results, even for low frequency and concentration, as we demonstrate below. We restricted ourselves to 2D to lighten the computational load and discuss extensions to 3D later, although 2D backscattering is qualitatively similar to 3D<sup>16</sup>.

Consider an incident plane wave  $e^{ik(x-x_R-t)}$ , where  $k$  is the wavenumber of the background medium, and we non-dimensionalise by taking the phase velocity of the background to be 1. The total wave  $u = e^{ik(x-x_R-t)} + u_b$  satisfies the 2D scalar wave equation, where  $u_b$  is the backscattered wave from the particles within the half-space  $x > 0$  and  $(x_R, 0)$  is the receiver position, such as shown in Figure 1. We use  $a$  for particle radius,  $n$  for number of particles per unit area (concentration) and  $\phi = a^2\pi n$  for volume fraction, and consider media where

$$1\% \leq \phi \leq 21\%, \quad 0.2 \leq a \leq 2.0 \quad \text{and} \quad 0 \leq k \leq 1. \quad (1)$$

For random media it is convenient to use the moments

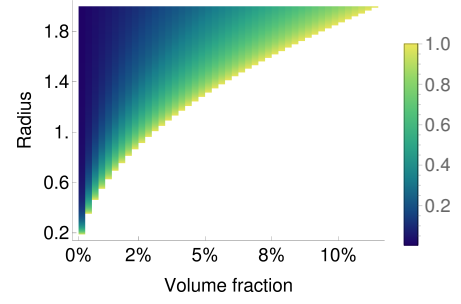


Figure 2: the density plot of  $|\langle u_b \rangle|$ , the absolute value of the mean backscattering, for  $k = 0.1$  and incident wave  $e^{ik(x-x_R-ct)}$  predicted by<sup>10</sup>. The white regions are where  $|\langle u_b \rangle| > 1$ , which is unphysical.

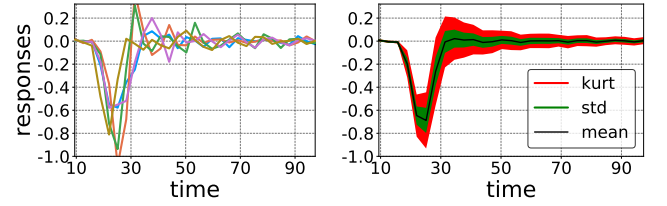


Figure 3: the backscattering in time from particles of radius  $a = 0.2$  occupying  $\phi = 20\%$  of the volume. Left, backscattering from five different configurations. Right, the moments of 756 configurations. The height of the black line is  $\langle u \rangle$  the mean response, while the total thickness of the green and red regions are the second  $\langle u_b \rangle_2$  (standard deviation) and fourth  $\langle u_b \rangle_4$  (kurtosis) moment.

of  $u$ . That is, if  $\Lambda$  represents one configuration of particles, then  $u = u(\Lambda)$  depends on  $\Lambda$  and its ensemble average is  $\langle u \rangle = \int u(\Lambda)p(\Lambda)d\Lambda$ , where  $p(\Lambda)$  is the probability of the particles being in the configuration  $\Lambda$ , then the central moments are

$$\langle u \rangle_n = \langle (u - \langle u \rangle)^n \rangle^{1/n}. \quad (2)$$

When we refer to a medium, we mean a material with a fixed particle radius and concentration. So that each medium is associated with a set of moments  $\langle u \rangle$  and (2).

There are many specialised methods to determine these moments<sup>10,17–20</sup>. Those that accurately calculate  $\langle u_b \rangle_j$  for a broad frequency range require  $\langle u_b \rangle$ , and a common approximation of  $\langle u_b \rangle$  for small volume fraction<sup>21</sup> is  $\langle u_b \rangle \approx i\phi(\pi a^2 k^2)^{-1}f(\theta)e^{-ikx}$ , where  $f(\theta) = -\sum_n e^{in\theta} J_n(ka)/H_n(ka)$  is the far-field scattering pattern. However, this approximation diverges when  $a \rightarrow 0$  and leads to the unphysical result  $|u_b| > 1$ , for every  $\phi$ . Even one of the most rigorous methods<sup>10</sup>, deduced for moderate concentration, presents the same problem, see Figure 2. This issue persists even for penetrable particles where  $u \approx 0$  on the boundaries of the particles.

To accurately determine all the moments over the range (1), we use the multi-pole method<sup>22</sup> to calculate  $u(\Lambda)$  for each configuration  $\Lambda$ , from which we determine

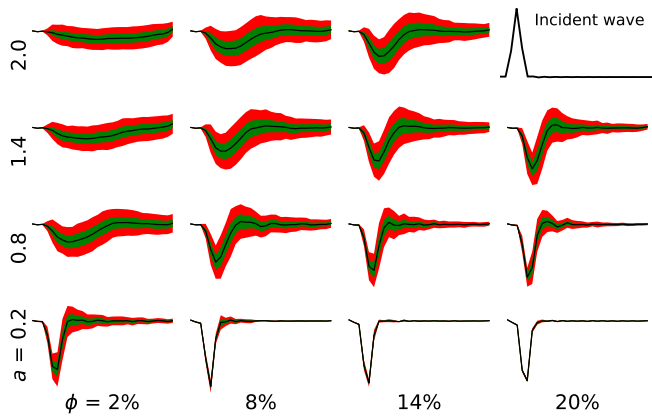


Figure 4: an overview of the moments, where each graph shows  $-1 < y < 0.35$ , while the  $x$ -axes shows time  $9.5 \leq t \leq 98$ . Each column has the same volume fraction  $\phi$ , while each row has the same particle radius  $a$ , except in the top-right which is the incident wave, shown to the same scale as the moments, but with time  $-9.5 \leq t \leq 78$  and  $-0.35 < y < 1.0$ .

the  $\langle u \rangle_n$ . The alternative would be to piece together different theoretical methods, whose range of validity is not clear<sup>14</sup>. In all convergence tests, truncation errors and benchmarks we were within 1% accuracy for each simulation. In the supplementary material we explain how to reproduce our results, including high performance software to simulate the backscattering<sup>23</sup> and implement the machine learning.

Accurately calculating the backscattering from an infinite halfspace, with a limited computational domain, is challenging. To overcome this challenge we calculate the backscattering of the incident time pulse  $e^{0.1(x-x_R-t)^2}$ , which for  $0 \leq k \leq 1$  gives a pulse with less than 1% Gibbs phenomena, and receive the backscattering at  $(x_R, 0)$ . By only receiving the signal for  $t \leq 98$ , we can exclude from the simulation all particles that would take more than  $t = 100$  for their first scattered wave to arrive at the receiver  $x_R$ . So we choose to calculate the backscattering for  $9.5 \leq t \leq 98$ , at which point  $u(x_R, 0, t) = u_b(x_R, 0, t)$  because the incident wave has already left. And as the largest wavenumber is  $k = 1$ , the smallest time step for the discrete Fourier transform is  $dt \approx \pi$ , which leaves us with 29 points on each backscattered wave. See Figure 3 for the incident time pulse and for  $\langle u \rangle$ ,  $\langle u \rangle_1$  and  $\langle u \rangle_4$ , where we include  $\langle u \rangle_4$  as it is known to be sensitive the micro-structure<sup>20,24</sup>.

In total we simulated the moments of 205 different media, evenly sampled from (1), which required 83000 backscattering simulations - each corresponding to one configuration  $\Lambda$ . For the larger simulations up to 7600 particles were used. To estimate the quality of the calculated moments, we used the standard error of the mean. See Figure 4 for an overview of the simulated moments.

**Learning from backscattering** — With a high quality data set of backscattered waves, we can now use

supervised machine learning to select a *model* that best explains the data. We then use this model to predict the concentration and the radius. Our supervised machine learning method of choice is kernel ridge regression<sup>25,26</sup>, which is very effective for fitting continuous processes, because when using continuous kernels they can fit any continuous function<sup>27</sup>. This allows us to establish whether the radius or the concentration are functions of  $\langle u \rangle$  or  $\langle u \rangle_2$  or both. In other words, we can determine which moments are needed to predict the radius and concentration. We present the results for concentration, instead of volume fraction, because it can be accurately predicted from just  $\langle u \rangle$ .

Our *training* set is the simulated backscattered moments of 205 different media. We say we *train* a model when using machine learning to select that model based solely on the training set. To determine the *predictive power* of our model, we generate a *test set* with 81 randomly chosen media with radius  $0.2 \leq a \leq 2.0$  and volume fraction  $1\% \leq \phi \leq 21\%$ . Every medium of the test set is distinct from the training set. All the parameters of the model were determined automatically using a 7-fold cross validation over the training set. To measure the goodness of fit, we use the  $R^2$  coefficient with respect to the mean of the test set. If  $R^2 = 0$  then the model has the same predictive power as the mean of the test set, while  $R^2 = 1$  shows that the model has perfect prediction. Finally we tested two continuous kernels, the Gaussian (or radial basis) and the Ornstein-Uhlenbeck kernel. Both kernels gave similar scores through cross-validation, though the Ornstein-Uhlenbeck kernel had a slightly better  $R^2$  coefficient on the test set, so we only report these results.

To begin, we train two models using only the first moment  $\langle u \rangle$ , one to predict the concentration and one to predict the radius, see the top graphs of Figure 5. This figure shows the scatter plot of the true concentration and radius of the test set against the predicted concentration and radius, respectively. The model for the concentration has an almost perfect prediction, with an  $R^2$  coefficient of 0.96. On the other hand, the model for the radius resulted in almost meaningless predictions with an  $R^2$  coefficient of 0.53. The failure of the first moment alone to predict radius is significant, since this indicates that the radius is not a continuous function of the first moment.

To accurately predict the radius, the second moment was necessary. Indeed, training a model on the first and second moment resulted in an accurate prediction of the radius with  $R^2 = 0.93$ , see Figure 5.

To show that our results, such as the top right of Figure 5, are not due to insufficient data, but likely extend beyond our data set, we examine the learning curves. A *learning curve* shows the  $R^2$  coefficient of a model as the quality of the data is increased. For example, if it was possible to predict the radius from an exact dataset of  $\langle u \rangle$ , then the model's  $R^2$  coefficient would increase when improving the training data's quality. Contrary to this, if

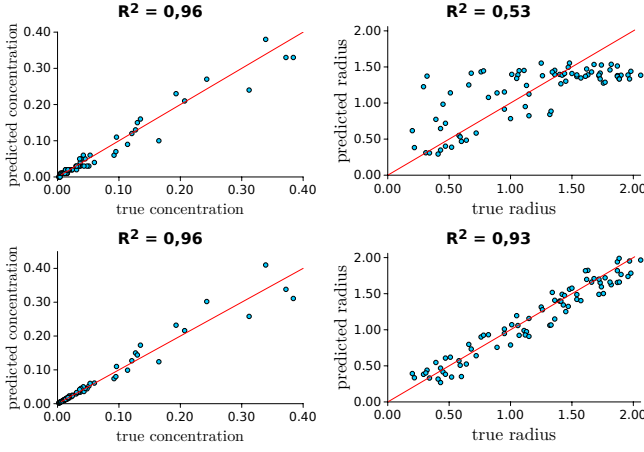


Figure 5: the scatter plots of the predicted against the true concentration and radius. The top two kernel models were trained using only the mean  $\langle u \rangle$ , while the bottom two were trained using the mean  $\langle u \rangle$  and second moment  $\langle u \rangle_2$ . Though the best result for predicting the concentration gives  $R^2 = 0.98$ , which results from using low wavenumbers, discussed later.

the  $R^2$  coefficient does not increase, or worst still there is no clear trend, then the model is incapable of predicting the radius, no matter the quality of the training data.

We vary the quality of the training data by changing: the number of media, the number of simulations for each medium, and by limiting the maximum wavenumber  $k$  of the incident wave. For every change in the training data we do a 7-fold cross validation. The resulting learning curves are shown in Figures 7 and 6, where for Figure 6 we limited the maximum wavenumber  $k$  of both the training and test set. The graphs on the left, in all these figures, we see that  $R^2$  does not tend to 1 when increasing the training data quality. The simplest explanation for this is that  $\langle u \rangle$  by itself is not enough to accurately predict the radius. However, the concentration is accurately predicted from  $\langle u \rangle$  even when using either 30% of the number of training media, having large standard errors of the mean, or using only wavenumbers  $k \leq 0.1$ . In fact limiting  $0 \leq k \leq 0.1$ , leads to an  $R^2 = 0.98$  for the concentration. On the other hand, when including the mean and second moment, shown by the graphs on the right of Figures 7 and 6, the learning curves for the radius clearly converge to  $R^2 = 1$ .

Finally, from Figure 6, we see that the learning curve saturates around a maximum wavenumber of 0.8. This indicates that  $0 < k < 0.8$  is the ideal range to measure particles in the range  $0 < a < 2$ . And that neither theory, simulation or experiments need go beyond  $ka = 1.6$ . Figure 8 shows what would be the smallest wavelength in this case, compared with the particle radiuses. Although to measure more details of the particles geometry, it is likely that  $ka > 1.6$  will be required.

**Conclusions** — By using supervised machine learning we showed that 1) the concentration can be predicted

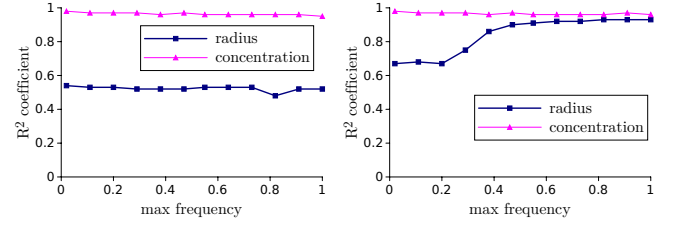


Figure 6: The  $R^2$  coefficient of the radius and concentration as we increase the maximum wavenumber  $k$  in the training data. That is, for each point  $(x, y)$ , we limit the incident wavenumbers of the training and test set to  $0 \leq k \leq x$ , which results in  $y = R^2$ . On the left (right) we used a model trained on only  $\langle u \rangle$  ( $\langle u \rangle$  and  $\langle u \rangle_2$ ).

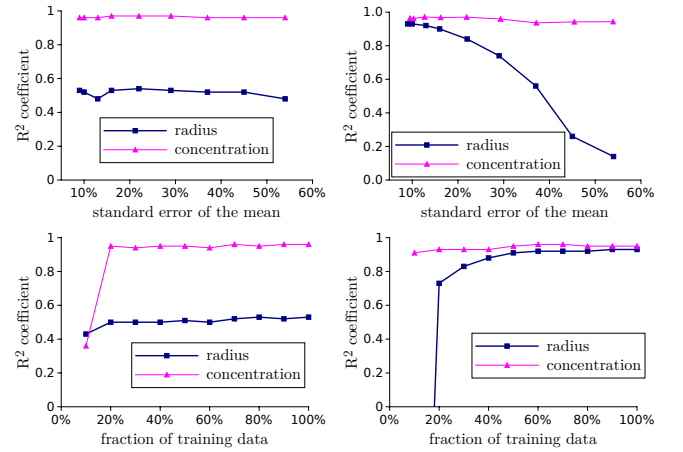


Figure 7: shows how the  $R^2$  coefficient of the radius and concentration change when changing the quality of the training data, while the test set was fixed with a relative standard error of the mean of 10%. The top two graphs increase the number of simulations per medium, resulting in a change of the relative standard error of mean  $\langle u \rangle$  on the  $x$ -axis. The bottom graphs increase the number of media, shown as a percentage of the full training data on the  $x$ -axis. The model on the left (right) was trained using only  $\langle u \rangle$  ( $\langle u \rangle$  and  $\langle u \rangle_2$ ).

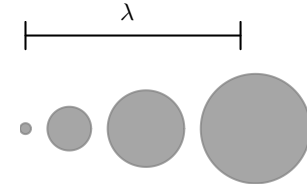


Figure 8: Compares smallest wavelength necessary,  $\lambda = 2\pi/0.8$ , to measure all particle radius's. The particles shown have radiuses 0.2, 0.8, 1.4, and 2.0. Clearly multiple scattering encodes sub-wavelength information<sup>28</sup>.

from the mean backscattering, though 2) the particle radius cannot be accurately predicted using the mean backscattering alone, but requires 3) the mean and second moment to accurately predict the radius, and 4) that the incident wavenumbers  $0 < k < 0.8$  need to be considered to accurately measure the radius's  $0 < a < 2$ , but that 5) to predict the concentration requires only  $k < 0.1$ . Our predictions for both the radius and concentration were accurate, with  $R^2 = 0.93$  and  $R^2 = 0.96$ , even though the standard error of the mean of the training and test set were 10%, see the top graphs of Figure 7. The backscattered signal were also sampled coarsely in time, with only 29 points on each signal. These imprecisions are promising, because it indicates that it may be possible to accurately measure particle size and concentration using receivers with limited resolution and limited number of backscattering measurements.

To extend our approach to other settings computational efficiency is important. Simulating the backscattered moments would be faster if the multilevel Monte Carlo methods<sup>29</sup> and fast multipole methods<sup>30</sup> were used. With this combination our approach could be applied to 3D spheres or to a wider parameter range. For instance, it may be possible to measure the physical properties of the particles, as well as the size and concentration. Another avenue to create more backscattering data is to piece together different theoretical models, which could then be validated with simulated near surface backscattering.

A.L. Gower, W.J. Parnell and I.D. Abrahams are grateful for the funding provided by EPSRC (EP/M026205/1). R.M. Gower is grateful for funding provided by the FSMP at the INRIA - SIERRA project-team.

## Supplementary material on learning about random media from near-surface backscattering

**Calculating near-surface backscattering** — We choose the multi-pole method because it takes advantage of the symmetry of the circular particles, making it computationally efficient, it is very accurate and it has hardly any artefacts<sup>22</sup>. It has been the method of choice for other packages dedicated to multiple scattering<sup>31</sup>, and can be made computationally efficient with the fast multi-pole method<sup>30</sup>. As this method is well established, here we only give a brief outline. Our code<sup>23</sup> was implemented in Julia<sup>32</sup>, a language focused on high performance numerics, and is open source<sup>33</sup>. All the tests and benchmarks we refer to are reproduced in the example and test folder.

The  $j$ -th particle scatters a wave  $u^j$ , which satisfies the 2D scalar wave equation  $\nabla^2 u^j + k^2 u^j = 0$ , and therefore has the form

$$u^j = \sum_{m=-M}^M A_m^j J_m(ka) \frac{H_m(kr^j)}{H_m(ka)} e^{im\theta^j} \quad \text{for } r^j \geq a, \quad (\text{S1})$$

where  $(r^j, \theta^j)$  are the polar coordinates of  $(x, y)$  centred at the  $j$ -th particles centre  $(x_j, y_j)$  and  $M$  is chosen so that (S1) converges. The  $H_m$  and  $J_m$  are Hankel and Bessel functions of the first kind, and the  $A_m^j$  are to be determined from boundary conditions. Using the above, we write the backscattered wave in the form  $u_b = \sum_{j=1}^N u^j$ , where  $N$  is the number of particles, and then from the boundary conditions

$$u = 0 \quad \text{on } r^j = a \quad \text{for } j = 1, \dots, N,$$

where  $u = e^{ik(x-x_R-t)} + u_b$ , combined with Graf's addition theorem leads to

$$A_m^s + \sum_{n=-M}^M \sum_{\substack{j=1 \\ j \neq s}}^N A_n^j \frac{J_n(ka)}{H_n(ka)} H_{n-m}(kR^{js}) e^{i(n-m)\theta^{js}} = -i^m e^{ik(x^s - x_R)}, \quad (\text{S2})$$

for  $m = -M, \dots, M$  and  $s = 1, \dots, N$ , which we use to solve for the  $A_m^s$  and completely determine  $u_b$ . The point  $(x_s, y_s)$  is the centre of the  $s$ -th inclusion and  $(R^{js}, \theta^{js})$  are the polar coordinates of  $(x_s, y_s)$  centred at  $(x_j, y_j)$ .

After calculating the solution in the frequency domain  $\omega = k$  for  $0 \leq k \leq 1$ , we can calculate the backscattered response in time measured at  $(x_R, 0)$ , where we consider  $ak \leq 2$ . The smaller  $ak$ , the smaller  $M$  needs to be.

One notable challenge, is that we want to approximate the backscattering  $u_b$  from a infinite halfspace  $x > 0$  filled with particles. One option is to use a computational domain large enough for the backscattered signal to converge. This issue of convergence is rarely discussed in the literature<sup>16,34–36</sup>. In our numerical experiments, on

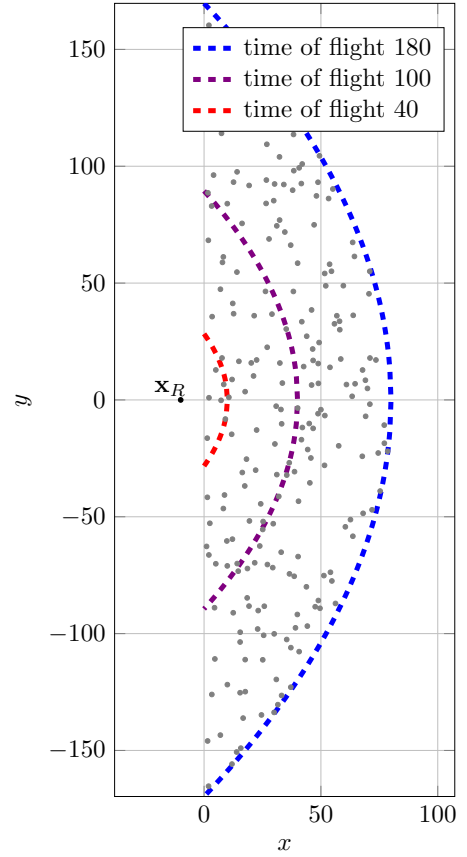


Figure S1: shows particles randomly placed according to a uniform distribution. For a plane incident wave to travel from  $x = -10$  to any point on the blue dashed curve and then directly back to the receiver  $\mathbf{x}_R$  takes time  $t = 180$ . Likewise for the purple/red curve it takes  $t = 120/60$ .

the order of  $10^4$  particles are needed before the backscattering converges within 1%. This becomes particularly challenging when  $ka \approx 1$  or larger, because  $M$  needs to increase. We find a simple solution is to calculate the backscattering in time  $t$  and keep only the early arrival  $t < 98$ . That why we exclude contributions from particles further away from the surface, where it takes longer than  $t = 100$  for their first scattered wave to return to the receiver  $\mathbf{x}_R = (x_R, 0)$ . This allows us to only simulate the response from particles near the surface, see Fig. S1 for an illustration. The backscattering in time from all the particles to the left of the blue dashed line is shown by the blue curve in Figure S2, and likewise for the purple/red curve. All three backscatterings are the same up to  $t = 40$ , as it takes  $t > 40$  for scattered wave from the closest particle above the red curve in Figure S1 to arrive. The same rationale explains why the blue and purple curves are the same for  $t < 100$ .

For the backscattered signal to converge within 1% accuracy required a 1800 mesh points for the wavenumber evenly sampled in  $0 \leq k \leq 2$ . This is because the finer the



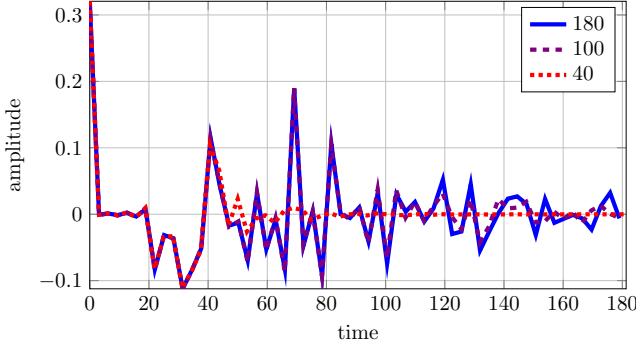


Figure S2: the backscattered waves in time from particles to the left of the blue, purple and red dashed lines in Figure S1

mesh, the longer the time period of the discrete Fourier transform of the backscattered waves. And a long time period is necessary because, due to multiple scattering, the backscattering can last a long time. On the contrary, if the time period considered is too short, the discrete Fourier transform will no longer be causal<sup>37</sup>.

**Learning from backscattering** — To train our models to predict the radius and concentration, we use  $L$  simulated media where  $(r_\ell, v_\ell) \in \mathbb{R}^2$  is the particle radius and the concentration of the  $\ell$ -th media. Let  $\langle u^\ell \rangle_j$  be the  $j$ th centred moment of the simulated backscattered waves on the  $\ell$ th media, and let

$$(\mathbf{M}^\ell) := \{\langle u^\ell \rangle_j \mid j = 1, 2, \dots, m\},$$

be the collection of  $m \in \mathbb{N}$  moments. We will refer to  $(\mathbf{M}^\ell, r_\ell, v_\ell)$  as the *training set* throughout. For the results presented in the article we used only the mean backscattering  $\langle u \rangle_1 = \langle u \rangle$ ,  $m = 1$ , or the mean and second moment,  $m = 1, 2$ , of the backscattering in the training set.

**Kernel ridge regression** — Our objective is to train  $h^r : \mathbf{M}^\ell \rightarrow h^r(\mathbf{M}^\ell) \in \mathbb{R}_+$  and  $h^v : \mathbf{M}^\ell \rightarrow h^v(\mathbf{M}^\ell) \in \mathbb{R}_+$  to predict the radius and concentration, respectively. In kernel ridge regression, these have a parametric form

$$h^r(\mathbf{M}) = \sum_{\ell=1}^L \alpha_\ell^r K(\mathbf{M}^\ell, \mathbf{M}),$$

and

$$h^v(\mathbf{M}) = \sum_{\ell=1}^L \alpha_\ell^v K(\mathbf{M}^\ell, \mathbf{M}),$$

where  $K : (\mathbf{M}', \mathbf{M}) \rightarrow \mathbb{R}$  is a given kernel function,  $\alpha_\ell^r$ , and  $\alpha_\ell^v$  for  $\ell = 1, \dots, L$  are the parameters that need to be determined. Let  $\mathbf{K} := \left( K(\mathbf{M}^n, \mathbf{M}^\ell) \right)_{n\ell}$  be the kernel matrix,  $\boldsymbol{\alpha} := (\alpha_\ell)_{\ell=1}^L$ ,  $\mathbf{r} := (r_\ell)_{\ell=1}^L$  and  $\mathbf{v} := (v_\ell)_{\ell=1}^L$ . We calculate the unknown parameter vectors  $\boldsymbol{\alpha}$  by minimizing the  $L^2$  loss over the training set. For instance, to

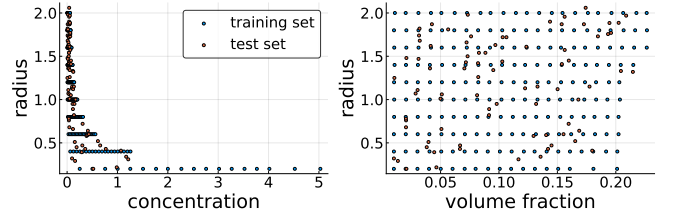


Figure S3: On the left (right) we have the concentration and radius (volume fraction and radius) of each medium in the training set (in blue) and test set (in red).

determine the parameters  $\alpha_\ell^r$  of the  $h^r$  model we solve

$$\boldsymbol{\alpha}^r = \arg \min_{\boldsymbol{\alpha} \in \mathbb{R}^L} \frac{1}{2L} \|\mathbf{K}\boldsymbol{\alpha} - \mathbf{r}\|_2^2 + \frac{\lambda_r}{2} \langle \mathbf{K}\boldsymbol{\alpha}, \boldsymbol{\alpha} \rangle, \quad (\text{S3})$$

where  $\lambda_r > 0$  is the regularization parameter. Analogously we introduce a regularization parameter  $\lambda_v$  for the  $h^v$  model.

The kernels we tested in our experiments are the following.

Gaussian	$K(\mathbf{M}, \mathbf{M}') = \exp \left( \frac{-\ \mathbf{M} - \mathbf{M}'\ ^2}{2\sigma^2} \right)$
Ornstein-Uhlenbeck	$K(\mathbf{M}, \mathbf{M}') = \exp \left( \frac{-\ \mathbf{M} - \mathbf{M}'\ }{\sigma} \right)$
Linear	$K(\mathbf{M}, \mathbf{M}') = \text{Tr} \left( \mathbf{M}^\top \mathbf{M}' \right),$

(S4)

where  $\sigma > 0$  is the kernel parameter.

**Testing the models** — To validate our models, we produced a test set of media with randomly chosen radii and concentrations, none of which are part of the training set. Let  $(\mathbf{M}^t, r_t, v_t)$  for  $t = 1, \dots, T$  be this test set, see Figure S3 for a scatter plot comparing the training set and test set.

To measure the goodness of fit of our models, we use  $R^2$ , the R squared coefficient of determination, over the test set. For example, let  $\hat{r}_t = h^r(\mathbf{M}^t)$  be the predicted radii for  $t = 1, \dots, T$ , and let  $\bar{r} = \sum_{t=1}^T r_t$  be the average radius over the test, then

$$R^2 = 1 - \frac{\sum_{t=1}^T (\hat{r}_t - r_t)^2}{\sum_{t=1}^T (\bar{r} - r_t)^2}.$$

If  $R^2$  is close to 1, then the  $\hat{r}_t$  are significantly better at predicting the true radii in comparison to using the mean  $\bar{r}$  as the predicted radius. Otherwise, if  $R^2$  is close to zero or even negative, then the predicted  $\hat{r}_t$  are worse than using the mean  $\bar{r}$ .

**Implementation details** — The code for the kernel ridge regression<sup>38</sup> based on moments was implemented in the Julia programming language, where we also show how to calculate the moments from the full simulated data. The parameters  $\lambda_r$ ,  $\lambda_v$  and  $\sigma$  were all determined using a 7-way cross-validation over the training set. No parameters were hand picked.

We also carried out standard data pre-processing including, normalizing and centring the data. We also applied the natural logarithm to the radius and concentration in the training set. Thus to recover a predicted radius and concentration, we apply exponentiation. This explicitly enforces that the models predicts a positive radius and concentration.

A.L. Gower, W.J. Parnell and I.D. Abrahams are grateful for the funding provided by EPSRC (EP/M026205/1). R.M. Gower is grateful for funding provided by the FSMP at the INRIA - SIERRA project-team.

## REFERENCES

- <sup>1</sup>R. E. Challis, M. J. W. Povey, M. L. Mather, and A. K. Holmes, “Ultrasound techniques for characterizing colloidal dispersions,” **68**, 1541–1637.
- <sup>2</sup>P. D. Thorne and D. Hurther, “An overview on the use of backscattered sound for measuring suspended particle size and concentration profiles in non-cohesive inorganic sediment transport studies,” **73**, 97–118.
- <sup>3</sup>P. Hu and J. A. Turner, “Contribution of double scattering in diffuse ultrasonic backscatter measurements,” **137**, 321–334.
- <sup>4</sup>D. P. Winebrenner, L. Tsang, B. Wen, and R. West, “Sea-ice characterization measurements needed for testing of microwave remote sensing models,” **14**, 149–158.
- <sup>5</sup>O. Torres, P. K. Bhartia, J. R. Herman, Z. Ahmad, and J. Gleason, “Derivation of aerosol properties from satellite measurements of backscattered ultraviolet radiation: Theoretical basis,” **103**, 17099–17110.
- <sup>6</sup>M. Almasian, T. G. Leeuwen, and D. J. Faber, “OCT amplitude and speckle statistics of discrete random media,” **7**, 14873.
- <sup>7</sup>J. Yi, A. J. Radosevich, J. D. Rogers, S. C. P. Norris, R. apolu, A. Tafove, and V. Backman, “Can OCT be sensitive to nanoscale structural alterations in biological tissue?” **21**, 9043–9059.
- <sup>8</sup>D. J. Pine, D. A. Weitz, J. X. Zhu, and E. Herbolzheimer, “Diffusing-wave spectroscopy: dynamic light scattering in the multiple scattering limit,” **51**, 2101–2127.
- <sup>9</sup>R. Weser, S. Wckel, B. Wessely, and U. Hempel, “Particle characterisation in highly concentrated dispersions using ultrasonic backscattering method,” **53**, 706–716.
- <sup>10</sup>P. A. Martin, “Multiple scattering by random configurations of circular cylinders: Reflection, transmission, and effective interface conditions,” **129**, 1685–1695 ().
- <sup>11</sup>J.-M. Conoir and A. N. Norris, “Effective wavenumbers and reflection coefficients for an elastic medium containing random configurations of cylindrical scatterers,” **47**, 183–197.
- <sup>12</sup>M. Caleap, B. W. Drinkwater, and P. D. Wilcox, “Effective dynamic constitutive parameters of acoustic metamaterials with random microstructure,” **14**, 033014.
- <sup>13</sup>A. Tourin, A. Derode, P. Roux, B. A. van Tiggelen, and M. Fink, “Time-dependent coherent backscattering of acoustic waves,” **79**, 3637.
- <sup>14</sup>A. Tourin, M. Fink, and A. Derode, “Multiple scattering of sound,” **10**, R31–R60.
- <sup>15</sup>M. Rupp, A. Tkatchenko, K.-R. Mller, and O. A. von Lilienfeld, “Fast and accurate modeling of molecular atomization energies with machine learning,” **108**, 058301.
- <sup>16</sup>B. Galaz, G. Haat, R. Berti, N. Taulier, J.-J. Amman, and W. Urbach, “Experimental validation of a time domain simulation of high frequency ultrasonic propagation in a suspension of rigid particles,” **127**, 148–154.
- <sup>17</sup>M. I. Mishchenko, L. D. Travis, and A. A. Lacis, *Multiple Scattering of Light by Particles: Radiative Transfer and Coherent Backscattering* (Cambridge University Press).
- <sup>18</sup>R. Snieder, “Coda wave interferometry and the equilibration of energy in elastic media,” **66**, 046615.
- <sup>19</sup>J. Garnier and K. Slna, “Fourth-moment analysis for wave propagation in the white-noise paraxial regime,” **220**, 37–81.
- <sup>20</sup>P. Sheng, *Introduction to Wave Scattering, Localization and Mesoscopic Phenomena*, Vol. 88 (Springer Science & Business Media).
- <sup>21</sup>L. L. Foldy, “The multiple scattering of waves. i. general theory of isotropic scattering by randomly distributed scatterers,” **67**, 107.
- <sup>22</sup>P. A. Martin, *Multiple Scattering: Interaction of Time-Harmonic Waves with N Obstacles*, Vol. 107 (Cambridge University Press).
- <sup>23</sup>A. L. Gower and J. Deakin, “jondea/multiplescattering.jl: Version 0.1,” (2017).
- <sup>24</sup>H. Ammari, J. Garnier, W. Jing, H. Kang, M. Lim, K. Slna, and H. Wang, *Mathematical and Statistical Methods for Multistatic Imaging*, Lecture Notes in Mathematics, Vol. 2098 (Springer International Publishing) DOI: 10.1007/978-3-319-02585-8.
- <sup>25</sup>B. E. Boser, I. M. Guyon, and V. N. Vapnik, “A training algorithm for optimal margin classifiers,” in *Proceedings of the Fifth Annual Workshop on Computational Learning Theory, COLT ’92* (ACM, New York, NY, USA, 1992) pp. 144–152.
- <sup>26</sup>M. A. Aizerman, E. A. Braverman, and L. Rozonoer, “Theoretical foundations of the potential function method in pattern recognition learning,” in *Automation and Remote Control*, Automation and Remote Control, No. 25 (1964) pp. 821–837.
- <sup>27</sup>C. A. Micchelli, Y. Xu, and H. Zhang, “Universal kernels,” *Journal of Machine Learning Research* **6**, 2651–2667 (2006).
- <sup>28</sup>F. Simonetti, “Multiple scattering: The key to unravel the sub-wavelength world from the far-field pattern of a scattered wave,” **73**, 036619.
- <sup>29</sup>M. B. Giles, “Multilevel monte carlo methods,” **24**, 259–328.
- <sup>30</sup>Y. J. Zhang and E. P. Li, “Fast multipole accelerated scattering matrix method for multiple scattering of a large number of cylinders,” **72**, 105–126.
- <sup>31</sup>D. W. Mackowski and M. I. Mishchenko, “A multiple sphere t-matrix fortran code for use on parallel computer clusters,” *Polarimetric Detection, Characterization, and Remote Sensing*, **112**, 2182–2192.
- <sup>32</sup>J. Bezanson, A. Edelman, S. Karpinski, and V. B. Shah, “Julia: A fresh approach to numerical computing,” *SIAM review* **59**, 65–98 (2017).
- <sup>33</sup>jondea, “MultipleScattering.jl: A julia library for simulating, processing and plotting multiple scattering of waves,” Version 0.1.
- <sup>34</sup>M. Chekroun, L. Le Marrec, B. Lombard, and J. Piroux, “Time-domain numerical simulations of multiple scattering to extract elastic effective wavenumbers,” **22**, 398–422.
- <sup>35</sup>V. J. Pinfield and R. E. Challis, “Simulation of incoherent and coherent backscattered wave fields from cavities in a solid matrix,” **132**, 3760–3769.
- <sup>36</sup>K. Muinonen, M. I. Mishchenko, J. M. Dlugach, E. Zubko, A. Penttil, and G. Videen, “Coherent backscattering verified numerically for a finite volume of spherical particles,” **760**, 118.
- <sup>37</sup>R. G. Lyons, *Understanding Digital Signal Processing*, 3rd ed. (Prentice Hall).
- <sup>38</sup>R. M. Gower, “MultipleScatteringLearnMoments: A julia library for learning the radius and concentration of a material by using the moments of simulated backscattered waves. the backscattered waves are generated..” Original-date: 2017-12-22T22:13:21Z.